Nanoscale

Accepted Manuscript

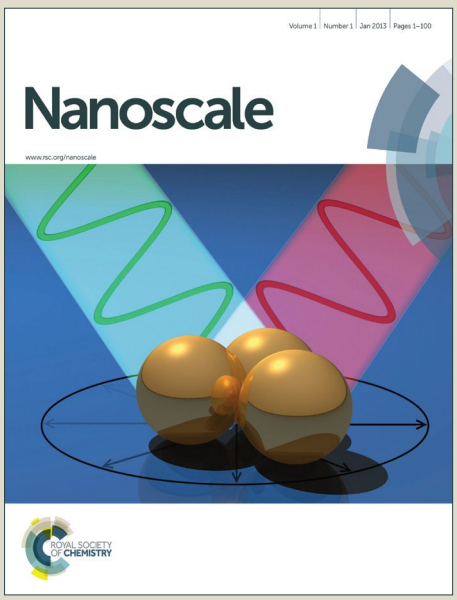

ROYAL SOCIETY OF CHEMISTRY

www.rsc.org/nanoscale

Nanoscale

ARTICLE

Morphology and Crystallinity Control of Ultrathin TiO_2 Layers Deposited on Carbon Nanotubes by Temperature-Step Atomic Layer Deposition

Received 1st April 2015,
Accepted 16th April 2015

DOI: 10.1039/x0xx00000x

www.rsc.org/

Carlos Guerra,[a] Yucheng Zhang,[b] Meng Li,[c] Vipin Chawla,[a] Rolf Erni,[b] Johann Michler,[a] Hyung Gyu Park,[c] and Ivo Utke[a,*]

Carbon nanotubes (CNTs) coated with titanium oxide (TiO_2) have generated considerable interest over the last decade and become a promising nanomaterial for a wide range of energy applications. The efficient use of the outstanding electrical properties of this nanostructure relies heavily on the quality of the interface and the thickness and morphology of the TiO_2 layer. However, complete surface coverage of the chemically inert CNTs and proper control of the morphology of the TiO_2 layer have not been achieved so far. Here, we report a new strategy to obtain ultrathin TiO_2 coatings deposited by "Temperature-step" Atomic Layer Deposition (TS-ALD) with complete surface coverage of non-functionalized multiwall carbon nanotubes (MWCNTs) and controlled morphology and crystallinity of the TiO_2 film. This strategy consists in adjusting the temperature during the ALD deposition to obtain the desired morphology. Complete coverage of long non-functionalized MWCNTs with conformal anatase layers were obtained by using a low temperature of 60°C during the nucleation stage followed by an increase to 220°C during the growth stage. This resulted in a continuous and amorphous TiO_2 layer, covered with a conformal anatase coating. Starting the deposition at 220 °C and reducing to 60 °C resulted in sporadic crystal grains at the CNT/TiO_2 interface covered with an amorphous TiO_2 layer. The results were accomplished through an extensive study of nucleation and growth of titanium oxide films on MWCNTs of which a detailed characterization is presented in this work.

Introduction

Carbon nanotubes (CNTs) coated with titanium oxide (TiO_2) have become a promising hybrid nanomaterial for a wide range of applications. From photocatalysis,[1-5] gas sensors,[6-8] to dye-sensitized solar cells[9-12] and energy storage.[13] These nanostructures combine the high surface area, excellent thermal and electrical conductivity of the CNTs, with the high photoactivity, chemical stability, environmentally friendliness, and versatility of TiO_2. The outstanding electrical properties of these nanocomposites, specifically the improved electron charge transport for efficient collection, is largely controlled by the quality of the interface between them, as well as the structural and morphological properties of the metal oxide coating.[14] Recent studies which have incorporated CNT/TiO_2 nanostructures for a hybrid photoanode in dye-sensitized solar cells have proved the approach to be a promising alternative to enhance charge transport kinetics of electrons towards the current collector.[15-18] This is accomplished by taking advantage of the high electrical conductivity of the CNTs to use them as electron highways. However, only small improvements of the energy conversion efficiency have been achieved mainly because of the short circuit and high recombination rates caused by the exposed surfaces of the CNTs to the electrolyte. Exposed surfaces of the CNTs –as a result from the poor coverage of the metal oxide– act as leakage pathways for electrons traveling through the CNTs, leading to a decrease of the overall electrical performance of the nanomaterial.[19] For this reason, complete surface coverage of the CNTS and a high quality interface between these materials are needed. Carbon nanotubes are generally known among other features for the chemically inert surfaces. The chemically inert carbon walls restrict the nucleation of a TiO_2 coating, leading to poor coverage of the CNTs. It is generally accepted that nucleation and growth of metal oxides initiate preferably at defect sites of the CNTs, where OH groups can chemisorb.[20, 21] For this reason, chemical and/or physical pre-treatments of CNTs are common methods to improve the TiO_2 coverage by introducing

[a] EMPA, Swiss Federal Laboratories for Materials Science and Technology, Laboratory for Mechanics of Materials and Nanostructures, Feuerwerkerstrasse 39, CH-3602 Thun, Switzerland. E-mail: ivo.utke@empa.ch
[b] EMPA, Swiss Federal Laboratories for Materials Science and Technology, Electron Microscopy Center, Überlandstrasse 129, CH-8600 Dübendorf, Switzerland
[c] ETH Zürich, Nanoscience for Energy Technology and Sustainability, Department of Mechanical and Process Engineering, Sonneggstrasse 3, Zürich CH-8092, Switzerland

† Electronic Supplementary Information (ESI) available: Additional TEM and SEM images, EDX mapping of the TiO_2 coverage along the cross-section of the MWCNTs, the XPS spectra of the C 1s and O 1s peak of the va-MWCNTs after 300 cycles of H_2O and a discussion about the expected thickness against the measured thickness of TS-ALD samples are presented in the supplementary information. See DOI: 10.1039/x0xx00000x

new functional groups and/or defects.[22, 23] However, these defects introduce more recombination sites for electrons and holes, and it has been proven to be detrimental to the original electrical properties of the CNTs.[24, 25] The deposition technique and process parameters play a crucial role to control not only the coverage of the CNTs but also the crystal structure, thickness, and morphology of the metal oxide layer. Therefore a process that induces the least amount of structural damage to the as-prepared CNTs is desired to keep their inherent electrical conductivity, as well as to ensure complete coverage of the CNT surface in order to prevent electrons traveling through the CNT to leak through the uncoated surfaces.

Atomic Layer Deposition (ALD) offers several advantages to deposit TiO_2 on CNTs compared with other more common techniques (e.g., sol-gel and hydrothermal deposition) such as homogenous and conformal coatings with a controlled thickness at an atomic level on geometrically complex nanostructures with high aspect ratios.[26, 27] Most of the previous studies of ALD TiO_2 coated carbon nanotubes have used functionalization methods prior to deposition. These studies have reported homogenous amorphous films at low temperatures[16, 22, 28-30] and rough anatase surfaces at high temperatures.[30] To the best of our knowledge, only few reports have used non-functionalized CNTs. Zhang *et al.* have reported incomplete coverage of the CNTs at 200°C with crystalline TiO_2 until a ~20 nm-thick rough film coalesced, leading to good coverage of the pristine CNTs.[21] TiO_2 deposited at 100°C using TDMAT and O_3 resulted in poor coverage of the carbon nanotubes.[31] Recently Hsu *et al.* showed homogenous films of ALD TiO_2 using $TiCl_4$ for photodection devices, however, there is no analysis of the ALD deposition process.[32]

In this study, we used non-functionalized vertically aligned multiwall carbon nanotubes (va-MWCNTs) and studied the nucleation and growth of TiO_2 films deposited by ALD using Titanium Tetra-Isopropoxide (TTIP) and water. By understanding how TiO_2 nucleates and grows on the carbon walls at different temperatures led us to a simple strategy to control the TiO_2 coverage on the CNTs, the morphology and crystallinity of the film. This strategy consists of adjusting the temperature at the different stages of nucleation and growth. The resulting films were characterized by scanning electron microscopy (SEM), transmission electron microscopy (TEM), Raman spectroscopy and X-ray photoelectron Spectroscopy (XPS).

Experimental

Synthesis of va-MWCNTs

A 20-nm-thick film of Al_2O_3 was deposited via Atomic Layer Deposition on a bare Si wafer as a support and then a 2-nm-thick film of Fe was deposited via e-beam evaporation atop as catalyst. Multiwalled carbon nanotube (MWCNT) growth was carried out in a cold-wall CVD reactor (Black Magic™, Aixtron). Catalyst substrate was loaded in the CVD chamber, evacuated below 200 mbar and then heated up to 770 °C at 300 °C/min, with 600 sccm of H_2 and 400 sccm of Ar flow rate. After annealing at the same temperature for 15 min, additional C_2H_4 (150 sccm) was turned on to start growth at 720 mbar total pressure. Upon completion of growth step, the reactor was cooled down to room temperature in Ar atmosphere. The va-MWCNTs had a length of ~150 µm.

The va-MWCNTs grown on Si substrates are far easier to handle to perform ALD coatings and different characterization techniques compared to other formats such as powder. In addition, they can be easily transferred to FTO substrates by a simple stamping technique[9] for future electrical characterization and device fabrication.

Deposition of ALD TiO_2

The samples were transferred into a built-in ALD reactor. Deposition of TiO_2 on va-MWCNTs was performed at a reactor temperature of 60°C, 120°C, and 220°C with an alternating precursor mixture of Titanium Tetra-Isopropoxide (TTIP) $Ti(OCH(CH_3)_2)_4$ heated to 90°C and H_2O at 40°C. The vapor delivery lines leading to the reactor were kept at 90°C. One ALD cycle consisted of a TTIP pulse of 10 s followed by a 40 s exposure to ensure more than enough time for diffusion and chemisorption, then purging with Ar for 60 s. Afterwards, H_2O was pulsed for 8 s with an exposure time of 40 s and purging of 60 s. The Ar flow was set to 50 sccm for both pulsing and purging steps which gave a background pressure of 0.26 mbar. The pulsing times used for TTIP and water, ensured the complete coverage of TiO_2 from top to bottom of the va-MWCNTs. Shorter pulsing times did not coat completely the long va-MWCNTs down to the bottom. We found that shorter exposure times had no effect on the coverage of the CNTs, however, the exposure time aids to extend or reduce the total time-length of the experiment. For nucleation studies 20 cycles were performed and 300 cycles to study the growth and morphology of TiO_2.

Based on the results obtained from these parameters, the Temperature-step (TS) experiments were performed with the same cycle times but the temperature changed during the deposition of 300 cycles as follows. TS-ALD 60°C-220°C: 60°C for the first 60 cycles (1-60), 120°C for the next 60 cycles (61-120), and 220°C for the remaining 180 cycles (121-300). TS-ALD 220°C-60°C: 220°C for the first 30 cycles (1-30), and changed to 60°C for the remaining 170 cycles (31-300); the temperature at the reactor reached 60°C at the 50th cycle.

Characterization of va-MWCNT/TiO_2

SEM images of the cross-section were acquired using a high resolution scanning electron microscope (Hitachi S4800, Japan) after cleaving the samples in half and analysing the cross-section.

TEM samples were prepared by dispersing the CNTs in methanol, ultrasonification for 5 minutes and pipetting a few droplets of the solution onto a carbon film. TEM was conducted on a JEOL2200FX microscope operated at 200 KeV. High-resolution TEM (HR-TEM) imaging and selected area

diffraction pattern (SADP) were performed in the TEM mode. Bright field (BF) and high-angle annular dark field (HAADF) imaging in the scanning TEM (STEM) mode. Small exposure time was used to avoid beam-induced damage or phase transformation.

Raman spectroscopy was performed in dry conditions using an upright Raman microscope (Nova Spectra, ND-MDT, Russia) featuring a laser source with a wavelength of 532 nm and a 50x objective with a numerical aperture of 0.75. Spectra were recorded at a spectral resolution of 2.7 cm^{-1} and the exposure time was 30 sec for all the samples. The use of a neutral density filter kept the laser power below 100 µw so that it does not induce phase transformation of TiO_2 or modify the MWCNT bands.[33] We observed induced phase transformation of amorphous TiO_2 into anatase by increasing the laser power to ~2.6 mW. All the peaks were fitted with a Lorentzian function.

XPS measurements were performed in a *Quantum2000* from Physical Electronics using a monochromatized Al K_α source (1486.6 eV). The X-ray spot had a diameter of 150 µm and operated at a power of 30 W at 15 kV. A neutralizer gun was used at 1.3 V and 20 µA. The core level spectra were fitted using a nonlinear least-square line shape analysis after subtraction of a Shirley background. The spectra were aligned to the characteristic asymmetric peak of graphite structures at 284 eV, and a FWHM of 0.98 eV and 1.1 eV was used for sp^2 and sp^3 species, respectively.[34-36] All the components were fitted using a Gaussian-Lorentzian line-shape except for the sp^2 component, in which an asymmetric Doniach-Sunjic (DS) line-shape was used.[37]

Results and discussion

Nucleation of TiO_2 on MWCNTs

In our previous work, we showed that the nuclei density of TiO_2 on MWCNTs decreases with increasing temperature, in the investigated range of 160°C-240°C.[21]

From this premise, we investigated even lower ALD deposition temperatures, namely 60°C and 120°C, to compare the nucleation behaviour with a high temperature of 220°C, which is just below the decomposition temperature of TTIP.[38] Low-temperature ALD that favours amorphous TiO_2 has not been widely investigated, perhaps because the anatase phase is desired for many applications. Figure 1 shows the coverage of 20 ALD cycles of TiO_2 at the aforementioned temperatures.

At a deposition temperature of 60°C a semi conformal and continuous thin layer can already be observed with a thickness of ~1.3±0.2 nm which covers most of the MWCNT. The high angle annular dark field (TEM-HAADF) image of the 60°C sample shows a continuous layer of TiO2 (represented by the bright materials contrast) covering the MWCNT (the dark region). To the best of our knowledge, this layer could be the thinnest and most conformal film of TiO_2 on a MWCNT that has been reported up to date. At 120°C, several nuclei of ~1.4±0.2 nm in thickness and up to 3.5 nm in lateral size were deposited along the MWCNT. The TEM-HAADF image for this temperature shows uncovered CNT regions (dark) partially covered with half-ellipsoidal TiO_2 nuclei (bright). We calculated ~0.08 nuclei per nm^2. The deposition of TiO_2 at 220°C shows only sporadic nuclei with a more spherical shape of ~1.8±0.5 nm decorating the MWCNT with ~0.07 nuclei per nm^2.

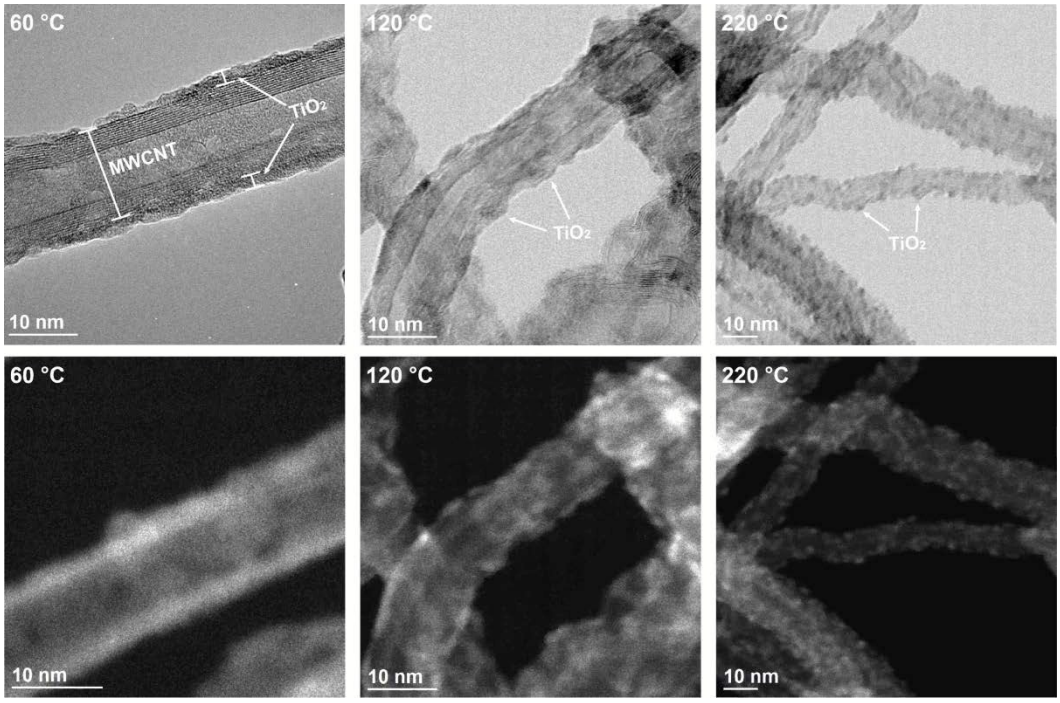

Figure 1. Nucleation density of 20 cycles of ALD TiO_2 on va-MWCNTs at different temperatures. The STEM-BF (top) and HAADF (bottom) images show that the nucleation density decreases as the deposition temperature increases. The bright contrast in the HAADF images is TiO_2.

At high temperature, the observed TiO_2 decoration functions as labelling points for defect sites, however for low temperature this is not the case. These results clearly indicate that effective coverage of TiO_2 is not only limited to the initial defect density of the MWCNTs. More TEM images for the deposition at 60°C are presented in Figure S1. Furthermore, the contact angle of the nuclei increases with deposition temperature and describes the subsequent growth mode. At 60°C, we have obtained a uniform and continuous coverage of TiO_2 along the MWCNTs, whereas at higher temperature, this lack of continuity enabled an island growth. Marichy *et al.* observed similar sporadic TiO_2 nuclei at 200°C which nucleated at the defects of the MWCNTs and attributed this effect to the defect density of the MWCNTs.[22] Meng *et al.* also reported similar nuclei at 250°C which grew and then coalesced as the number of cycles increased, displaying also the anatase phase; nonetheless their CNTs were functionalized.[30] The deposition at 60°C and 120°C did not show any sign of crystallinity as expected at these low temperatures. At 220°C we have observed crystalline TiO_2 nuclei (Figure S2).[21]

Raman spectroscopy was performed on the MWCNTs before and after the deposition of 20 cycles of TiO_2. Figure 2a shows the characteristic Raman-active modes of the MWCNTs in the region from 1000 cm^{-1} to 2000 cm^{-1} at an excitation wavelength of 532 nm. The G Mode (~1586 cm^{-1}) is due to planar vibrations from the hexagonal lattice of sp^2 carbon atoms of the MWCNTs. The D mode (~1343 cm^{-1}) corresponds to the amount of structural defects/disorder, such as amorphous carbon, vacancies and heteroatoms in the 2D hexagonal lattice. The D mode is also used as an indication of sp^2 to sp^3 transition of functionalized carbon atoms, and the D' mode (~1620 cm^{-1}) can arise from external induced defects such as bending of the inner/outer cylinders or by physical/chemical functionalization treatments.[39-41] The ratio between the D- and G-band (I_D/I_G) is widely used as an indication of the quality of the CNTs (i.e., structural imperfections) and the amount of sp^3 hybridization after functionalization of the CNTs. The small I_D/I_G ratio of the pristine va-MWCNTs indicates a low defect density. After the nucleation of TiO_2 there is an increase of the I_D/I_G ratio, which increased at lower deposition temperatures, being the highest at 60°C. It is important to note that temperature is not responsible for the increase of the D-band, as it has been shown that MWCNTs are stable in air up to 420°C and up to 1300°C in argon.[42] Furthermore, the D- and G-bands remain unchanged up to a temperature of >400°C.[42, 43] Therefore, the increase of the I_D/I_G ratio is due to the nucleation of TiO_2 on the MWCNTs and not temperature. The I_D/I_G ratio increased from 0.46 for the pristine MWCNTs to 0.61 at a deposition temperature of 60°C, and then it decreased to 0.58 at 120°C and to 0.56 at 220°C (Table 1). These results suggest a relatively higher amount of sp^3 hybridization of carbon atoms at lower ALD temperatures. This is complemented by a red shift and broadening of the D-band, indicating altogether the stress build-up on the outer carbon walls of the CNTs by a close interaction with TiO_2.[44] The contraction of the lattice spacing due to the formation of C-O-Ti bonds stretches the in-plane covalent bonds that results in a red shift of the D- and G-bands.[45-47] The maximum shift and increase of the FWHM is observed at an ALD deposition temperature of 60°C, wh[illegible] exhibited the highest MWCNT coverage.

In addition, XPS measurements showed a higher atomi[illegible] percentage of Ti deposited at 60°C (~5.3%) than at 120°C (3.9%) and 220°C (3.2%), from the ratio of Ti 2p, O 1s and C 1[illegible] The XPS spectra of the C 1s peaks from Figure 2b support the conclusion of an increase in the concentration of sp^3 carbon[illegible] and C-O bonding after ALD at low temperatures.

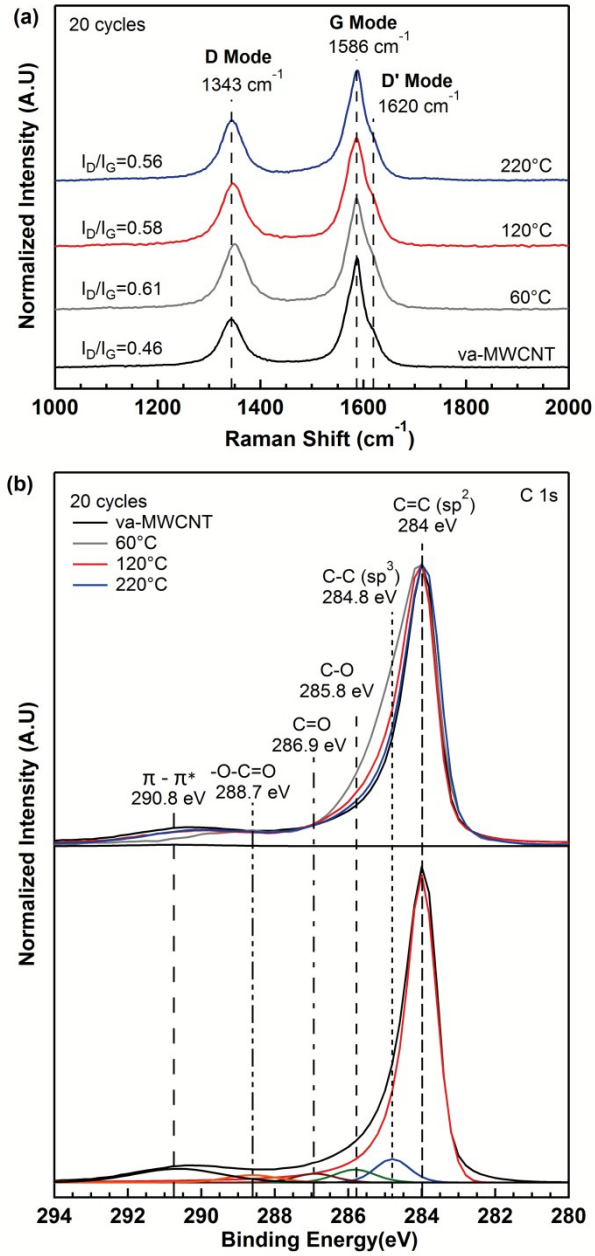

Figure 2. Interaction between the va-MWCNTs and TiO_2 after 20 cycles at differe[illegible] deposition temperatures measured by (a) Raman spectroscopy and (b) XPS. Rama[illegible] spectra show an increase of the I_D/I_G ratio with lower deposition temperatures which corresponds to the increase of sp^3 hybridized carbon atoms and C-O species from the C 1s peak in the XPS spectra.

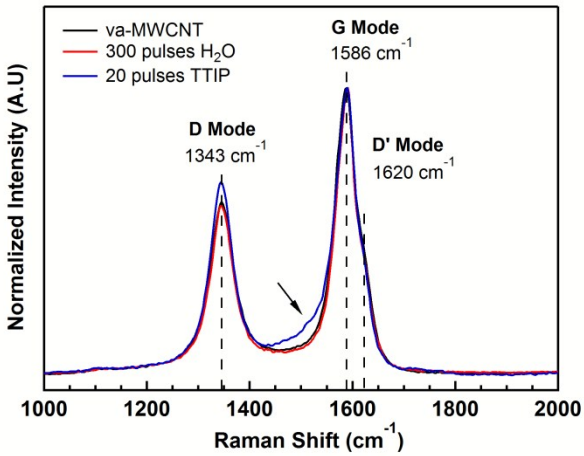

Figure 3. Interaction between the va-MWCNTs and 300 pulses of H_2O and 20 pulses of TTIP at 60 °C measured by Raman spectroscopy.

It is clear that the peaks, where the sp^3 carbons and C-O species are located, increased in percentage with decreasing ALD deposition temperature. We do not disregard the fact that at low temperatures carbon ligands from the TTIP precursor might still remain in the TiO_2 layer.[48, 49] In fact, it is known that alkoxide ligands from TTIP tend to form bridging structures[50] which might be the cause leading to the uniform coverage at low temperatures. These ligands may have attached to the CNTs through the adsorption of the oxygen atom (of the alkoxide ligand) during the first cycles. The adsorption of this oxygen atom to a bare silicon surface has been reported to be more energetically stable than binding to a hydroxyl group.[50]
To clear these doubts, we show in Figure 3, the Raman-active modes of one va-MWCNT sample subjected to 300 pulses of water alone, and other sample subjected to 20 pulses of TTIP alone, both at 60 °C. The Raman spectra clearly show an increase of the D-band and broadening of the G-band after 20 pulses of TTIP alone, meaning that TTIP is responsible for the sp^3 hybridization of the carbon atoms of the CNTs. The va-MWCNTs subjected to 300 cycles of water alone showed no substantial difference compared to the pristine sample, hence water is not responsible for sp^3 hybridization or C-O bonding (Figure S6). Therefore, the increase of the sp^3 species from the C 1s peak at 60 °C is indeed caused by the sp^2 to sp^3 transition of the carbon atoms from the outer walls, and the C-O groups could be a combination of both the C-O-Ti bonding at the interface and from the remaining C-O-Ti bonds from the alkoxide ligands. The Raman and XPS measurements are consistent with the TEM observations where at lower deposition temperature there is a higher coverage of the CNT surface and thus more sp^2 carbons have been transformed into sp^3, creating a C-O-Ti bonding at the interface.

Growth, Morphology and Crystallinity of TiO_2 on MWNCTs

In Figure 4, SEM and TEM images show the morphology and conformality of the titania layer on the va-MWCNTs after 300 cycles at different ALD temperatures. Interestingly, the most conformal and homogenous film was obtained at a temperature of 60 °C with a thickness of ~5 nm. At this temperature, the TiO_2 film exhibited a layered growth which started from the continuous nuclei deposited during the nucleation stage. At 120°C, the half-ellipsoidal nuclei grew in a nanoparticle network with a thickness variation of ~7-9 nm along the va-MWCNTs which resulted in a type of a "pearl necklace" structure. The sporadically distributed nuclei deposited at 220°C grew and coalesced, causing a rough morphology with a coating thickness as large as ~17-23 nm. Nevertheless, at this temperature, we observed uncoated areas of the MWCNTs (Figure S3), while almost none were observed at the lower temperatures. EDX performed on the cross section of the ~150 µm long va-WMCNTs confirms the TiO_2 coverage from the top to the bottom (Figure S4). The homogenous film obtained at 60°C was entirely amorphous, as expected at this low temperature. The TiO_2 nanoparticle network obtained at 120°C presented crystalline inclusions on the amorphous base layer (Figure S5) and the selected area diffraction pattern (SADP) inset showed weak diffraction patterns. The rough TiO_2 deposited at 220°C is almost entirely anatase. At 220°C, anatase crystal growth is thermodynamically favoured and initiated from the high density nuclei formed during the initial cycles and coalesced during growth. These observations are confirmed with Raman spectroscopy presented in the next sections. The measured GPC at 300 cycles increased from 60°C (~0.16 Å/cycle) to 120°C (~0.27±0.03 Å/cycle) and to 220°C (0.65±0.1 Å/cycle), which are in line with the trend of the ALD window. However, the GPC values obtained at 120°C and 220°C are slightly higher than those reported in literature.[30, 49, 51, 52]
The low GPC at < 200°C has been explained by Aarik *et al.* as low reactivity of water with TTIP.[49] The high growth per cycle at high temperatures is attributed to a greater reactivity of TTIP with water in combination of a preferred crystal growth as observed by recent studies.[51-55] These studies demonstrated that the higher GPC observed at high temperatures is caused by the larger density of hydroxyl groups at the surface of the crystal. Consequently, Reiners *et al.* have also observed a preferential crystallization of TiO_2 into anatase by extending the length of the ALD process even at low temperatures.[52] Furthermore, Mitchell *et al.* observed amorphous ALD TiO transform into anatase with a post-deposition hydrothermal treatment at 120°C in the lapse of one day.[56] It is important to highlight that the length of our ALD experiments were on the order of ~18hrs for 300 cycles. The time-temperature dependency of anatase crystallization, -which improves the hydroxyl group density and thus the GPC-, explains the reason why we have obtained anatase crystal inclusions at such a low temperature for crystallization of 120°C and the higher GPC was observed compared to other studies.[30, 48, 53] Therefore, by adjusting the experimental time-length at a certain temperature can affect the crystallization behaviour and thus the GPC. It appears that low-temperature ALD using TTIP and water enables a better control of the thickness.

For many applications of CNT/TiO_2 nanostructures the anatase phase is desired because of its higher photocatalytic activity.[57, 58] However, complete surface coverage of the CNTs is a m

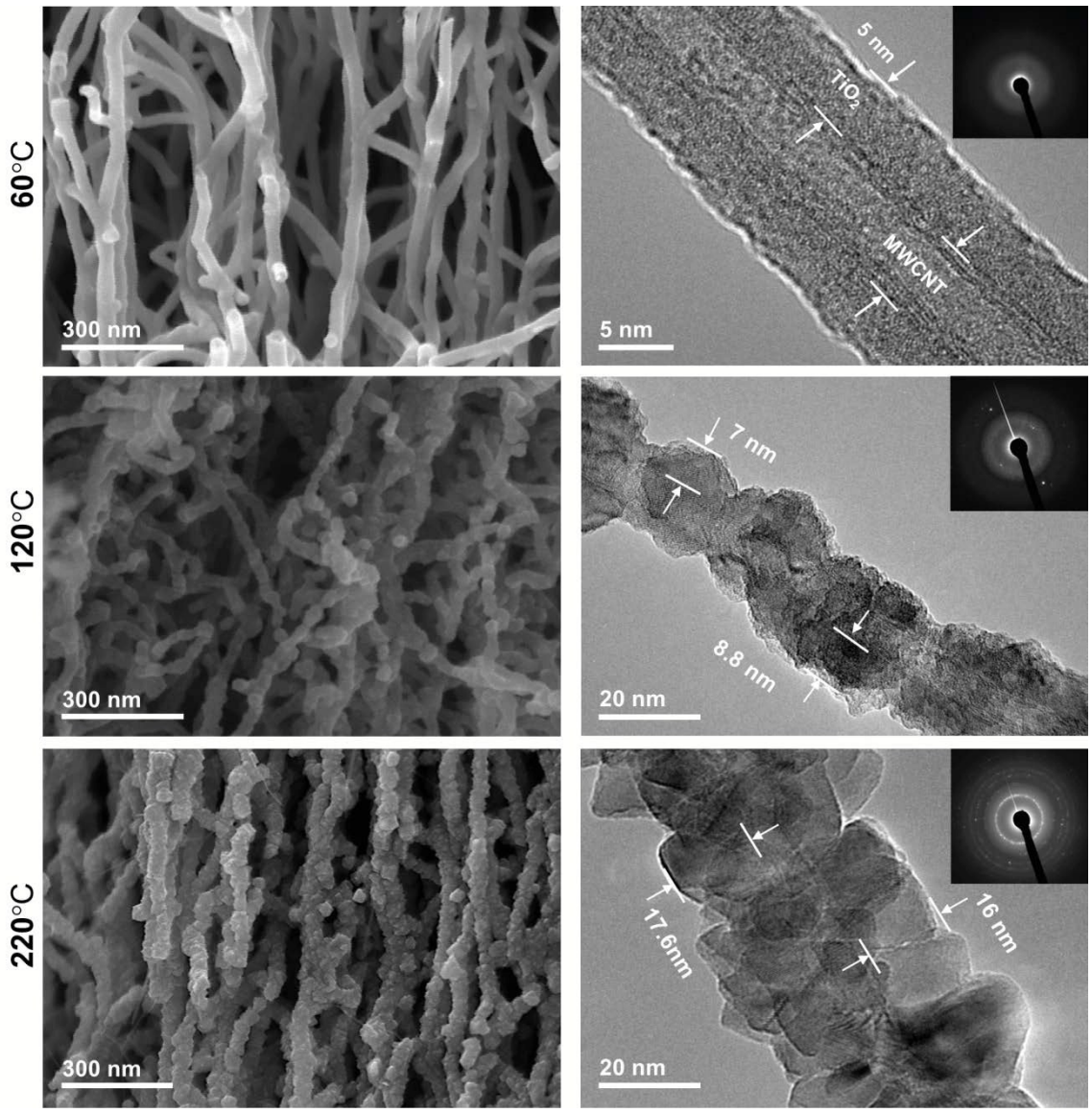

Figure 4. Morphology of 300 cycles of ALD TiO_2 on va-MWCNTs at different deposition temperatures. SEM images (left column) show the cross section of the MWCNTs after ea ALD deposition. TEM images (right column) of individual MWCNTs showing the morphology and conformality, the inset shows the SADP from the corresponding sample.

to prevent injected electrons to the CNTs to leak through the uncoated surfaces, which will obstruct their efficient collection Therefore, to achieve complete coverage of the CNTs without any pre-functionalization treatment can only be by ALD at low deposition temperatures during the nucleation stage. Nonetheless, higher temperatures are still required during the growth stage to obtain the anatase phase, that is, without recurring to any post-deposition heat treatment.

Temperature-step ALD

From the results presented so far, we can conclude that the nucleation stage will govern the initial coverage of TiO_2 and influence the final morphology. Consequently, the temperature at the succeeding growth stage will determine the crystallinity. Therefore, by adjusting the temperature in each of these stages during deposition, we obtain the desired nanostructure.

To test these hypotheses, we performed two experiment using a "Temperature-step ALD" strategy (TS-ALD): (i) Start th ALD deposition at 60°C for the initial 60 cycles to depos conformal and continuous film to completely coat the carbo nanotubes. Then, during the ALD deposition, increase th temperature to 120°C for the next 60 cycles to end at 220° for the remaining 180 cycles to obtain crystal growth (TS-ALD 60°C-220°C). (ii) Start the deposition at 220 °C for the first 3 cycles to deposit sporadic crystalline TiO_2 nuclei and the decrease the temperature to 60°C for the remaining cycles t conformally coat the crystalline grains with amorphous TiO_2 (TS-ALD 220°C-60°C).

The resulting morphologies are presented in Figure 5. The fina morphology of the TS-ALD 60°C-220°C sample consists of a conformal layer of TiO_2 similar to the one obtained at 60°C and does not display a rough morphology that could have been caused as a result of the crystal growth from the 220°C step.

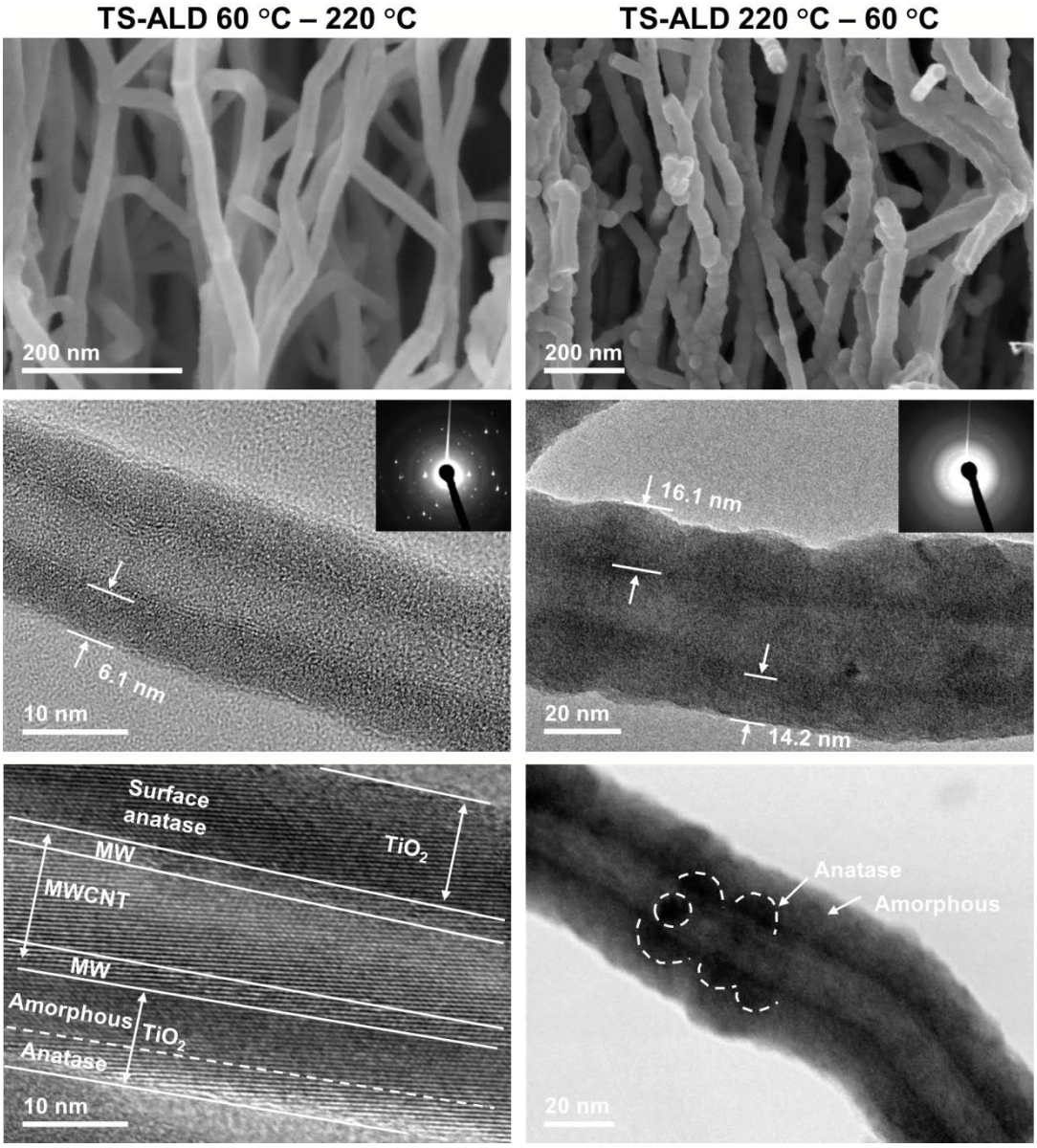

Figure 5. Morphology of 300 cycles of TiO_2 deposited by the Temperature-step process: TS-ALD 60°C-220°C (left) and TS-ALD 220°C-60°C (right). The SEM images (Top) show the cross section of the va-MWCNTs and the TEM images (middle) show the morphology and conformality; the inset shows the SADP from the corresponding sample. The HR-TEM (left bottom) and STEM (right bottom) images show the interface between the amorphous and anatase TiO_2 with the MWCNTs.

Nevertheless, as the SADP inset shows, the sample displays crystalline diffraction patterns from the crystal growth step at 220°C. The HR-TEM image shows an adhesion base layer of ~4 nm-thick amorphous TiO_2 deposited on the MWCNT and the interface with a ~2.1 nm-thick anatase layer. The interplanar distance calculated from the lattice fringes is 0.33 nm which corresponds to the (101) lattice plane of the anatase phase. These images reveal that the crystal growth started from the conformal amorphous TiO_2 base layer and followed the same initial conformal morphology. The temperature of 220°C during the time-length of the remaining 180 cycles was not sufficient to crystallize the entire amorphous base layer, though it was enough to deposit crystalline material at the surface. These results suggest that crystallization of TiO_2 might be more dependent on time and temperature in comparison to a "critical thickness", as suggested by other studies.[52] On the other hand, the TS-ALD 220°C-60°C sample display rather coarser layer with a thickness as large as ~14-16 nm. The coarse morphology is caused by the crystalline grai decoration formed during the nucleation stage at 220°C whic was covered by the amorphous layer deposited at 60°C durin the growth stage. The SADP inset show crystalline diffractio patterns which must be coming from the embedded cryst grains on the amorphous matrix. The STEM-HAADF imag shows these crystalline nuclei (darker regions) at the interfac with the CNT and an amorphous layer as the coating. Remarkably, the thickness obtained for both TS-ALD processe are similar to those results where the temperature used during the nucleation stage was kept constant during the whol process, such as 60°C (5 nm) and 220°C (~16-17.6 nm). Correspondingly, the measured thickness of 6.1 nm (TS-ALD 60°C-220°C) and ~14-16 nm (TS-ALD 220°C-60°C) do

coincide with the expected thicknesses of ~11.7 nm and ~7.3 nm, respectively (based on the isothermal GPC values given in the previous section). To elaborate, the expected thickness can be simplified as:

$$T = cycles\ (T_1) \cdot GPC\ (T_1) + cycles\ (T_2) \cdot GPC\ (T_2) + cycles\ (T_3) \cdot GPC\ (T_3)...$$

Where, T is the expected thickness of the added thicknesses obtained at each temperature-step. A detailed discussion is presented in the supporting information. To summarize, we have concluded that the difference in thickness is largely controlled by the first deposited layer, in this case, the amorphous TiO_2 and the crystalline grains deposited for the TS-ALD 60°C-220°C and TS-ALD 220°C-60°C, respectively. There is a competition between amorphous and crystal growth which affects the GPC. The amorphous TiO_2 base layer delayed the formation of an ordered anatase layer. Without crystallization there is no increase of hydroxyl groups at the crystal surface[51, 52] and therefore, no enhancement of the GPC. The opposite occurred to the TS-ALD 220°C-60°C sample. Hence, by adjusting the number of cycles and cycle time during the nucleation and growth stage at a given temperature, one can modify the deposition of amorphous and crystalline layers and thus the thickness of the coating.

Nevertheless, the final morphology would still be largely controlled by the initial morphology during the nucleation stage.

We used Raman spectroscopy to unambiguously identify the local order of crystalline TiO_2 materials.[59] Figure 6 compares the Raman-active modes of anatase TiO_2 of the different ALD temperature processes.

The Raman spectra show well-resolved anatase peaks for the samples with TiO_2 deposited at 220°C and TS-ALD 60°C-220°C at: $E_{g(1)}$ 144cm^{-1}, $E_{g(2)}$ 198cm^{-1}, $B_{1g(1)}$ 395cm^{-1}, $A_{1g}E_{1g(2)}$ 517cm^{-1} and $E_{g(3)}$ 636 cm^{-1}.[45, 53, 60] The deposition at 60°C does not show any signal from anatase due to its amorphous nature. At 120°C, there is a weak signal of anatase, mainly at $E_{g(1)}$, which corresponds to the crystalline inclusions of < 7 nm observed in TEM (Figure S5). The TS-ALD 220°C-60°C also shows a weak signal from the crystalline nuclei formed during the initial step at 220°C. The occurrence that the small crystallites appear to be isolated and embedded in amorphous TiO_2 suppresses the Raman signal. Furthermore, the red shift of the $E_{g(1)}$ band of both samples corresponds to a reduced anatase crystallite size.[61, 62]

The TS-ALD 60°C-220°C sample displays well-resolved anatase peaks even with a very thin layer of crystalline material compared to that of the ~17 nm thick layer of anatase deposited at 220°C . This is an indication that a considerable amount of a continuous anatase coating covering the amorphous base layer is present, and thus no red shift is observed.

In Figure 7 the Raman spectra show the active vibrations in the region of the MWCNTs after 300 cycles at each temperature process. The I_D/I_G ratio indicated in Figure 6 increased even further compared to the I_D/I_G ratios of the nucleation stage shown in Figure 2a. This could mean that there was more sp^3 hybridization of CNT carbon atoms during the growth of TiO_2.Especially, the depositions at 120°C and 220°C, there was not a complete coverage of the CNT surface after 20 cycles and subsequent cycles may have had increased the sp^3 concentration.

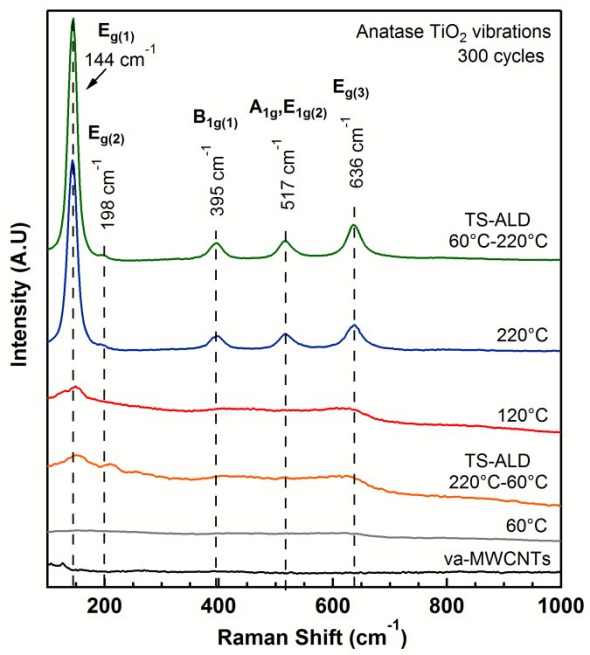

Figure 6. Raman-active modes of anatase TiO_2 at different ALD temperature processes.

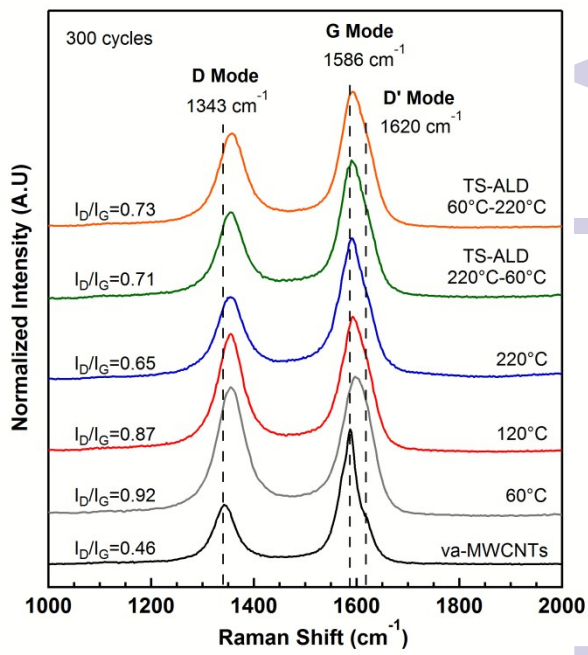

Figure 7. Interaction of TiO_2 with the va-MWCNTs measured by Raman spectroscopy after 300 cycles at different temperature processes.

Table 1. Raman peak positions, FWHM, I_D/I_G and $I_{D'}/I_G$ ratios after 20 and 300 cycles of TiO_2 at different deposition temperatures.

ALD Temp.	No. Cycles	D-band Position (cm^{-1})	D-band FWHM (cm^{-1})	G-band Position (cm^{-1})	G-band FWHM (cm^{-1})	D'-band Position (cm^{-1})	D'-band FWHM (cm^{-1})	I_D/I_G	$I_{D'}/I_G$
	Pristine	1343.4	51.2	1585.8	40.0	1620.0	12.4	0.46	0.10
60°C	20	1350.0	56.3	1586.6	43.7	1620.4	14.9	0.61	0.15
	300	1356.0	70.0	1596.4	61.0	1627.1	20.0	0.92	0.20
120°C	20	1346.7	55.8	1586.4	45.7	1620.3	17.0	0.58	0.16
	300	1354.4	61.8	1593.1	54.4	1622.0	20.4	0.87	0.21
220°C	20	1344.7	52.2	1586.2	47.5	1620.5	12.5	0.56	0.10
	300	1355.1	64.7	1591.4	58.1	1623.6	25.0	0.65	0.18
TS-ALD 60°C-220°C	300	1354.6	62.2	1588.7	53.4	1620.4	23.0	0.71	0.23
TS-ALD 220°C-60°C	300	1356.5	68.9	1591.9	55.2	1623.5	22.5	0.73	0.24

The reason why the I_D/I_G ratio at 220°C is lower than any other temperature can be explained by the fact that there are still uncovered CNT surfaces after 300 cycles, mainly due to the weak nucleation sites which lead to exposed CNT surfaces as we have observed from SEM images (Figure S2).

Other reason may be due to the island growth observed, which upon coalescence of the anatase crystals, the surface of the CNTs remain uncoated. A scheme of this event is portrayed in Figure 8c.

Both of the TS-ALD processes exhibited a similar I_D/I_G ratio comparable to those at low deposition temperatures. The I_D/I_G ratio from the TS-ALD 220°C-60°C sample is larger than the one obtained only at a deposition temperature of 220 °C. This shows that the amorphous layer deposited at 60 °C on the growth stage assisted to coat uncovered regions as a result from the sporadic nuclei formed at 200 °C. Furthermore, both the D- and G-bands red-shifted and broadened further after 300 cycles of TiO_2 at all the different deposition temperatures, which is altogether an indication of a strong interaction of the TiO_2 layer with the CNTs.[1, 45-47] The largest red shift and broadening is observed where low temperatures were involved in the ALD deposition and therefore the larger CNT surface coverage. It is therefore logic to assume that a larger CNT surface coverage will ensure a stronger interaction between these two materials. Table 1 shows the values for the position and FWHM of the Raman-active modes. These results will provide new insight to the analysis of charge transport kinetics in these nanostructures

Nucleation and Growth Mechanisms of TiO_2 on CNTs

Based on our results, we propose a model that further extends the knowledge of nucleation and growth of ALD TiO_2 on CNTs, to which we have incorporated our Temperature-step ALD studies (Figure 8). Low temperature ALD (i.e., 60 °C) enables a continuous and uniform coverage of TiO_2 on the MWCNTs, probably caused by the attachment of the alkoxide ligands to the CNTs. This layer grows into a conformal amorphous TiO_2 film (Figure 8a). At 60 °C, TTIP is less reactive with water and consequently there is a lower concentration of hydroxyl groups which reduces the GPC.

On the other hand, at higher temperatures, the very first molecules of TTIP react preferably at the defect sites of the CNTs, and subsequent cycles will continue to deposit only at those sporadic nuclei which provide the only available OH sites after every cycle. The large contact angle and spherical shape of the TiO_2 nuclei suggest that the incoming molecules of TTIP and H_2O react only at these sites without creating new bonding with the CNTs. The high temperature improves the reactivity of TTIP with water and, in combination with the time-length of the experiment, promotes the ordering of Ti-O that results in crystal growth which subsequently increases the density of hydroxyl groups at the surface, improving the GPC. The deposition performed at 120 °C presented anatase crystal inclusions due to the extended time of the ALD deposition, which promoted crystal growth and resulted in a nanoparticle network along the CNTs (Figure 8b). The ALD deposition at 220 °C resulted in a rough TiO_2 surface and large areas of uncoated CNTs due to the sporadic nucleation behaviour and subsequent island growth (Figure 8c).

The TS-ALD strategy takes advantage of the nucleation and growth mechanisms at different temperatures. Adjusting the temperature to 60°C during the nucleation stage followed by an increase to 220°C during the growth stage, resulted in a continuous and amorphous TiO_2 layer, covered with a conformal anatase coating (Figure 8d). Starting the deposition at 220 °C and then reducing to 60 °C resulted in sporadic crystal grains covered with a coarser amorphous TiO_2 layer (Figure 8d).

The TS-ALD approach provides a route to tailor the interface and control the thickness, crystal structure and morphology of the TiO_2 coating. At the nanoscale, these parameters become an important factor to improve the charge transport kinetics between these materials. For instance, the TiO_2 coating on the CNTs needs to be thin enough for efficient electron injection towards the CNTs. However, it has to be thick enough and completely coat the CNT surface to prevent the back transfer of electrons. Therefore, the optimal thickness will be a compromise between these two phenomena. The morphology plays also an important role. A coarser morphology, such as the one obtained for the TS-ALD 20 0°C-60°C sample, will increase the active surface area of the TiO_2 layer compared to a conformal coating, which is a valuable asset to increase the

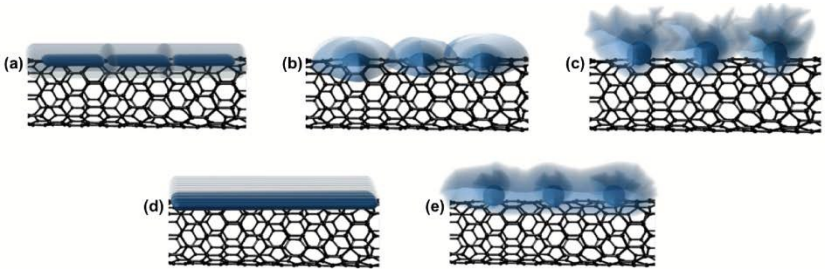

Figure 8. Nucleation and growth mechanisms of ALD TiO_2 on MWCNTs using TTIP and H_2O : (a) The ALD deposition at 60°C enables a continuous and uniform amorphous TiO_2 film on the MWCNTs (b) At 120°C, the half-ellipsoidal nuclei grew into a nanoparticle network along the MWCNTs with anatase crystal inclusions on the amorphous base layer. (c) At 220°C, the sporadic nuclei exhibited an island growth and coalesced, causing a rough morphology and exposed CNT surfaces. (d) The TS-ALD 60°C-220°C resulted in a continuous and amorphous TiO_2 layer, covered with a conformal anatase coating (e) The TS-ALD 220°C-60°C resulted in sporadic crystal grains covered with a coarser amorphous TiO_2 layer.

photocatalytic activity or the dye loading to improve dye-sensitized solar cells. As previously discussed, the anatase phase is also desired for many applications. However, the roughness that derives from the crystallization can affect the performance of the device, and post-deposition heat treatments introduce undesired stress effects to the parent material, such as in MEMS devices.[63] The TS-ALD strategy could be a solution to this problem. The proper control of the interface and the TiO_2 coating at the nanoscale will exploit the exceptional electrical properties of many nanostructures, allowing for a straight forward analysis of the charge transport kinetics between two materials.

Conclusions

We have successfully developed a new strategy to deposit continuous and conformal TiO_2 ultrathin films with complete surface coverage of non-functionalized va-MWCNTs. With this strategy, we have also gained control over the morphology, thickness and crystallinity of the TiO_2 coating. This strategy consists in tuning the temperature on the different phases of nucleation and growth during the ALD deposition. Starting the ALD deposition at 60 °C enables the complete and continuous coverage of the CNTs with an amorphous ultrathin film. We have demonstrated through Raman spectroscopy and XPS measurements that TTIP deposited at low temperatures is responsible for the complete and continuous coverage of the MWCNTs and therefore have a stronger interaction with the CNTs. XPS measurements showed an increased concentration of sp^3 and C-O species from the C 1s peak after the deposition of 20 ALD cycles of TiO_2 at 60 °C. The C-O signal arises from the combination of alkoxide ligands that may have remained in the film and C-O-Ti bonding at the interface. This conclusion is supported by Raman spectroscopy showing an increase of sp^3 hybridized carbon atoms (I_D/I_G ratio) and broadening of the G-band of the MWCNTs after 20 pulses of TTIP alone.

The ability of the alkoxide ligands to form bridging structures may have facilitated the adsorption of the TTIP molecule to the carbon walls which resulted in a continuous and conformal layer of TiO_2 in the following cycles. Subsequently, by increasing the temperature to 220 °C during the growth stage we have obtained a conformal anatase coating covering the amorphous layer. TEM images showed the interface between the amorphous adhesion layer and the anatase coating. The crystalline phase was confirmed by Raman spectroscopy showing well-resolved peaks for the anatase vibrations. On the other hand, starting the deposition at 220 °C, we deposited sporadic crystalline anatase grains on the CNTs, and upon lowering the temperature to 60 °C during the growth stage, an amorphous layer was deposited, embedding the crystal grains which resulted in a coarser morphology. The final TiO_2 thickness obtained using the TS-ALD strategy will be largely controlled by the first deposited layers. The high GPC observed at high temperatures in our samples, we attribute to the time-temperature dependency for crystallization which increases the hydroxyl groups and improves the GPC.[51, 52] At low temperatures, amorphous TiO_2 is favoured and thus exhibits a better control of the thickness. Therefore, by adjusting the number of cycles and the time-length in each of the stages, at a given temperature, will determine the thickness of the amorphous and anatase layers to tailor the desired thickness and morphology. The thickness, crystal structure and surface morphology of thin films become an important factor to improve the electrical performance of these nanostructures. The "Temperature-step" strategy will be also by of high interest to deposit other metal oxides, where the interface and morphology need to be tailored.

Acknowledgements

We acknowledge the financial support of the SNF funding under the Sinergia project CRSII2_147615/1 and EMPA COFUND fellowship scheme funded by the Marie Curie action of the European Commission.

References

1. J. Yu, T. Ma and S. Liu, *Phys. Chem. Chem. Phys.*, 2011, **13**, 3491-3501.
2. S.-Y. Lu, C.-W. Tang, Y.-H. Lin, H.-F. Kuo, Y.-C. Lai, M.-Y. Tsai, H. Ouyang and W.-K. Hsu, *Appl. Phys. Lett.*, 2010, **96**, 231915.
3. B. Chai, T. Peng, X. Zhang, J. Mao, K. Li and X. Zhang, *Dalton Trans.*, 2013, **42**, 3402-3409.
4. Y. Cong, X. Li, Y. Qin, Z. Dong, G. Yuan, Z. Cui and X. Lai, *Appl. Catal. B: Environ.*, 2011, **107**, 128-134.

5. B. Gao, G. Z. Chen and G. Li Puma, *Appl. Catal. B: Environ.*, 2009, **89**, 503-509.
6. C. Marichy, N. Donato, M. Latino, M. G. Willinger, J. P. Tessonnier, G. Neri and N. Pinna, *Nanotechnology*, 2015, **26**, 024004.
7. E. Llobet, E. H. Espinosa, E. Sotter, R. Ionescu, X. Vilanova, J. Torres, A. Felten, J. J. Pireaux, X. Ke, G. Van Tendeloo, F. Renaux, Y. Paint, M. Hecq and C. Bittencourt, *Nanotechnology*, 2008, **19**, 375501.
8. N. Van Duy, N. Van Hieu, P. T. Huy, N. D. Chien, M. Thamilselvan and J. Yi, *Physica E*, 2008, **41**, 258-263.
9. N. Yazdani, D. Bozyigit, I. Utke, J. Buchheim, S. K. Youn, J. Patscheider, V. Wood and H. G. Park, *ACS Appl. Mater. Interfaces*, 2014, **6**, 1389-1393.
10. H. Abdullah, M. Z. Razali, S. Shaari and M. Raihan Taha, *Int. J. Photoenergy*, 2014, **2014**, 1-9.
11. A. Bahramian, *Ind. Eng. Chem. Res.*, 2013, **52**, 14837-14846.
12. K. T. Dembele, G. S. Selopal, C. Soldano, R. Nechache, J. C. Rimada, I. Concina, G. Sberveglieri, F. Rosei and A. Vomiero, *J. Phys. Chem. C*, 2013, **117**, 14510-14517.
13. K. Hemalatha, A. S. Prakash, G. K and M. Jayakumar, *J. Mater. Chem. A*, 2014, **2**, 1757.
14. Z. Li, B. Gao, G. Z. Chen, R. Mokaya, S. Sotiropoulos and G. Li Puma, *Appl. Catal. B: Environ.*, 2011, **110**, 50-57.
15. Y.-F. Chan, C.-C. Wang, B.-H. Chen and C.-Y. Chen, *Prog. Photovolt: Res. Appl.*, 2013, **21**, 47-57.
16. S. H. Jin, G. H. Jun, S. H. Hong and S. Jeon, *Carbon*, 2012, **50**, 4483-4488.
17. T. Y. Lee, P. S. Alegaonkar and J.-B. Yoo, *Thin Solid Films*, 2007, **515**, 5131-5135.
18. W. J. Lin, C. T. Hsu, Y. C. Lai, W. C. Wu, T. Y. Hsieh and Y. C. Tsai, *Adv. Mater. Res.*, 2011, **410**, 168-171.
19. J. Chen, B. Li, J. Zheng, J. Zhao and Z. Zhu, *J. Phys. Chem. C*, 2012, **116**, 14848-14856.
20. C. Marichy and N. Pinna, *Coord. Chem. Rev.*, 2013, **257**, 3232-3253.
21. Y. Zhang, C. Guerra-Nuñez, I. Utke, J. Michler, M. D. Rossell and R. Erni, *J. Phys. Chem. C*, 2015, DOI: 10.1021/jp511004h, 150203103227001.
22. C. Marichy, J.-P. Tessonnier, M. C. Ferro, K.-H. Lee, R. Schlögl, N. Pinna and M.-G. Willinger, *J. Mater. Chem.*, 2012, **22**, 7323.
23. K. Balasubramanian and M. Burghard, *Small*, 2005, **1**, 180-192.
24. N. M. A. B. Sulong, J. Sahari, R. Ramli, B. Deros, J. Park, *Eur. J. Sci. Res.*, 2009, **29**, 13-21.
25. F. Buffa, G. A. Abraham, B. P. Grady and D. Resasco, *J. Polym. Sci., Part B: Polym. Phys.*, 2007, **45**, 490-501.
26. S. M. George, *Chem. Rev.*, 2010, **110**, 111-131.
27. C. Marichy, M. Bechelany and N. Pinna, *Adv. Mater.*, 2012, **24**, 1017-1032.
28. A. Gomathi, S. R. C. Vivekchand, A. Govindaraj and C. N. R. Rao, *Adv. Mater.*, 2005, **17**, 2757-2761.
29. X. Sun, M. Xie, J. J. Travis, G. Wang, H. Sun, J. Lian and S. M. George, *J. Phys. Chem. C*, 2013, **117**, 22497-22508.
30. X. Meng, M. N. Banis, D. Geng, X. Li, Y. Zhang, R. Li, H. Abou-Rachid and X. Sun, *Appl. Surf. Sci.*, 2013, **266**, 132-140.
31. S. Deng, S. W. Verbruggen, Z. He, D. J. Cott, P. M. Vereecken, J. A. Martens, S. Bals, S. Lenaerts and C. Detavernier, *RSC Advances*, 2014, **4**, 11648.
32. C. Y. Hsu, D. H. Lien, S. Y. Lu, C. Y. Chen, C. F. Kang, Y. L. Chueh, W. K. Hsu and J. H. He, *ACS Nano*, 2012, **6**, 6687-6692.
33. L. Bokobza and J. Zhang, *Express Polymer Letters*, 2012, **6**, 601-608.
34. J. Filik, P. W. May, S. R. J. Pearce, R. K. Wild and K. R. Hallam, *Diamond Relat. Mater.*, 2003, **12**, 974-978.
35. S. Hussain, R. Amade, E. Jover and E. Bertran, *Nanotechnology*, 2012, **23**, 385604.
36. D. W. Lee and J. W. Seo, *J. Phys. Chem. C*, 2011, **115**, 2705-2708.
37. A. L. Hsu, R. J. Koch, M. T. Ong, W. Fang, M. Hofmann, K. K. Kim, T. Seyller, M. S. Dresselhaus, E. J. Reed, J. Kong and T. Palacios, *ACS Nano*, 2014, **8**, 7704-7713.
38. E. S. Filatov, H. Nizard, P. P. Semyannikov, S. V. Sysoev, S. V. Trubin, N. B. Morozova, K. V. Zherikova and N. V. Gelfond, 2009.
39. Q. H. Wang, Z. Jin, K. K. Kim, A. J. Hilmer, G. L. C. Paulus, C. J. Shih, M. H. Ham, J. D. Sanchez-Yamagishi, K. Watanabe, T. Taniguchi, J. Kong, P. Jarillo-Herrero and M. S. Strano, *Nat Chem.*, 2012, **4**, 724-732.
40. M. A. Ali, S. Srivastava, P. R. Solanki, V. Reddy, V. V. Agrawal, C. Kim, R. John and B. D. Malhotra, *Scientific reports*, 2013, **3**, 2661.
41. S. A. Curran, J. A. Talla, D. Zhang and D. L. Carroll, *J. Mater. Res.*, 2005, **20**, 3368-3373.
42. A. Mahajan, A. Kingon, Á. Kukovecz, Z. Konya and P. M. Vilarinho, *Mater. Lett.*, 2013, **90**, 165-168.
43. S. Osswald, E. Flahaut, H. Ye and Y. Gogotsi, *Chem. Phys. Lett.*, 2005, **402**, 422-427.
44. C.-H. Wu, C.-Y. Kuo and S.-T. Chen, *Environ. Technol.*, 2013, **34**, 2513-2519.
45. Y. Min, K. Zhang, W. Zhao, F. Zheng, Y. Chen and Y. Zhang, *Chem. Eng. J.*, 2012, **193-194**, 203-210.
46. Y. Yu, J. C. Yu, C.-Y. Chan, Y.-K. Che, J.-C. Zhao, L. Ding, W.-K. Ge and P.-K. Wong, *Appl. Catal. B: Environ.*, 2005, **61**, 1-11.
47. Y. R. Ahn, Y. S. Lee, A. A. Ogale, C. H. Yun and C. R. Park, *Fibers and Polymers*, 2006, **7**, 85-87.
48. Q. Xie, J. Musschoot, D. Deduytsche, R. L. Van Meirhaeghe, C. Detavernier, S. Van den Berghe, Y.-L. Jiang, G.-P. Ru, B.-Z. Li and X.-P. Qu, *J. Electrochem. Soc.*, 2008, **155**, H688.
49. J. Aarik, A. Aidla, T. Uustare, M. Ritala and M. Leskelä, *Appl. Surf. Sci.*, 2000, **161**, 385-395.
50. J.-M. Lin, A. V. Teplyakov and J. C. F. Rodríguez-Reyes, *J. Vac. Sci. Technol. A*, 2013, **31**, 021401.
51. S. K. Kim, S. Hoffmann-Eifert, M. Reiners and R. Waser, *J. Electrochem. Soc.*, 2011, **158**, D6.
52. M. Reiners, K. Xu, N. Aslam, A. Devi, R. Waser and S. Hoffmann-Eifert, *Chem. Mater.*, 2013, **25**, 2934-2943.
53. I. Dirnstorfer, H. Mähne, T. Mikolajick, M. Knaut, M. Albert and K. Dubnack, *J. Vac. Sci. Technol. A*, 2013, **31**, 01A116.
54. G. X. Liu, F. K. Shan, W. J. Lee and B. C. Shin, *J. Korean Phys. Soc.*, 2007, **50**, 1827-1832.
55. H. Zhou, C. Wang, Z. Feng, S. Li and B. Xu, *Surf. Coat. Technol.*, 2012, **207**, 34-41.

56. D. R. G. Mitchell, G. Triani and Z. Zhang, *Thin Solid Films*, 2008, **516**, 8414-8423.
57. J. A. Campbell, M. deBorniol, A. J. Mozer, P. J. Evans, R. P. Burford and G. Triani, *J. Vac. Sci. Technol. A*, 2012, **30**, 01A157.
58. T. Luttrell, S. Halpegamage, J. Tao, A. Kramer, E. Sutter and M. Batzill, *Scientific reports*, 2014, **4**, 4043.
59. I. M. Arabatzis, T. Stergiopoulos, D. Andreeva, S. Kitova, S. G. Neophytides and P. Falaras, *J. Catal.*, 2003, **220**, 127-135.
60. P. Clemens, X. Wei, B. L. Wilson and R. L. Thomas, *J. Comp. Mater.*, 2013, **03**, 21-32.
61. W. Zhou, K. Pan, Y. Qu, F. Sun, C. Tian, Z. Ren, G. Tian and H. Fu, *Chemosphere*, 2010, **81**, 555-561.
62. V. Likodimos, T. Stergiopoulos, P. Falaras, R. Harikisun, J. Desilvestro and G. Tulloch, *J. Phys. Chem. C*, 2009, **113**, 9412-9422.
63. Y. Huang, G. Pandraud and P. M. Sarro, *J. Vac. Sci. Technol. A*, 2013, **31**, 01A148.